Column-Integrated Moist Static Energy Budget Analysis on Various Time Scales during TOGA COARE

KUNIAKI INOUE AND LARISSA BACK

University of Wisconsin–Madison, Madison, Wisconsin

(Manuscript received 29 August 2014, in final form 29 January 2015)

ABSTRACT

Moist static energy (MSE) budgets on different time scales are analyzed in the TOGA COARE data using Lanczos filters to separate variability with different frequencies. Four different time scales (~2-day, ~5-day, ~10-day, and MJO time scales) are chosen based on the power spectrum of the precipitation and previous TOGA COARE studies. The lag regression-slope technique is utilized to depict characteristic patterns of the variability associated with the MSE budgets on the different time scales.

This analysis illustrates that the MSE budgets behave in significantly different ways on the different time scales. On shorter time scales, the vertical advection acts as a primary driver of the recharge–discharge mechanism of column MSE. As the time scale gets longer, in contrast, the relative contributions of the other budget terms become greater, and consequently, on the MJO time scale all the budget terms have nearly the same amplitude. Specifically, these results indicate that horizontal advection plays an important role in the eastward propagation of the MJO during TOGA COARE. On the MJO time scale, the export of MSE by the vertical advection is in phase with the precipitation. On shorter time scales, the vertical velocity profile transitions from bottom heavy to top heavy, while on longer time scales, the shape becomes more constant and similar to a first-baroclinic-mode structure. This leads to a more-constant gross moist stability on longer time scales, which the authors estimate.

1. Background

To investigate the relationship between tropical convection and its associated large-scale circulations, past work has examined column-integrated moist static energy (MSE) budgets. These budgets tell us about the processes associated with the growth and decay of column MSE. The column MSE is useful as a diagnostic quantity in the deep tropics primarily for two reasons. First, it is approximately conserved in moist adiabatic processes, and it is often beneficial to study any phenomenon from a perspective of conserved variables. Second, the column MSE is tightly connected to tropical convective variability. Column water vapor is known to be closely linked to precipitation anomalies in the tropics (e.g., Raymond 2000; Bretherton et al. 2004; Neelin et al. 2009; Masunaga 2012), and temperature anomalies are small owing to the large Rossby radius (Charney 1963, 1969; Bretherton and Smolarkiewicz 1989; Sobel and Bretherton 2000). Together, these two constraints mean that the evolution of column MSE is closely related to the evolution of precipitation anomalies. In this work, we explore the charging and discharging mechanisms of column MSE that are associated with precipitation anomalies for various frequencies of variability. To do this, we examine column MSE budgets using data from the Tropical Ocean and Global Atmosphere Coupled Ocean–Atmosphere Response Experiment (TOGA COARE; Webster and Lukas 1992) field campaign.

The column-integrated MSE budget equation is, following Yanai et al. (1973),

$$\frac{\partial\langle h\rangle}{\partial t} = -\langle \mathbf{v}\cdot\nabla h\rangle - \left\langle \omega\frac{\partial h}{\partial p}\right\rangle + \langle Q_R\rangle + \mathrm{SF}, \qquad (1)$$

where $h \equiv s + Lq$ represents MSE, s represents dry static energy (DSE), L represents the latent heat of vaporization, q represents specific humidity, Q_R represents radiative heating rate, SF represents surface fluxes of MSE, the other terms have conventional meteorology meanings, and we have neglected a residual due to ice processes. The angle brackets represent a vertical

Corresponding author address: Kuniaki Inoue, Department of Atmospheric and Oceanic Sciences, University of Wisconsin–Madison, 1225 W. Dayton St., Madison, WI 53706.
E-mail: inoue2@wisc.edu

DOI: 10.1175/JAS-D-14-0249.1

integral over mass in the troposphere. Because in the deep tropics variations in the temperature field are much smaller than those of moisture, variations in h are primarily due to fluctuations of atmospheric moisture. Thus, investigating the column h budget leads us to understand how moisture anomalies amplify and decay in the tropics.

Episodes of organized deep convection in the tropics are thought to generally begin with bottom-heavy diabatic heating[1] that progressively deepens as the convection develops and eventually becomes top heavy and stratiform. This structure has been seen in convectively coupled equatorial waves (e.g., Takayabu et al. 1996; Straub and Kiladis 2003; Haertel and Kiladis 2004; Haertel et al. 2008; Kiladis et al. 2009), the MJO (e.g., Lin et al. 2004; Kiladis et al. 2005; Benedict and Randall 2007; Haertel et al. 2008), and even individual mesoscale convective systems (e.g., Mapes et al. 2006). The vertical profile of convection also has a strong impact on numerical simulations of the MJO (e.g., Lin et al. 2004; Fu and Wang 2009; Kuang 2011; Lappen and Schumacher 2012, 2014), convectively coupled waves (e.g., Cho and Pendlebury 1997; Mapes 2000; Kuang 2008), and convective organization in general. These phenomena are presently very challenging to simulate correctly, which makes numerical weather prediction difficult (e.g., Lin et al. 2006; Kim et al. 2009; Benedict et al. 2013).

Interestingly, bottom-heavy profiles of vertical motion are associated with the import of MSE by the vertical circulation (i.e., $-\langle \omega \partial h/\partial p \rangle$). These tend to coincide with the buildup of moisture in disturbances. Conversely, top-heavy profiles of vertical motion are associated with the export of MSE by the vertical circulation and these tend to coincide with the decay of moisture in disturbances. This suggests that, as pointed out by Peters and Bretherton (2006), the vertical advection term could be playing a role in the charging and discharging of column MSE associated with disturbances. This was also seen to some degree in recent work on the MSE budget during the Dynamics of the Madden–Julian Oscillation (DYNAMO) field campaign (Sobel et al. 2014). In this work, we systematically examine the relative contribution of this vertical advective term as well as other terms to the buildup and decay of column MSE for various frequencies of variability observed during TOGA COARE.

We also examine hypotheses about MJO dynamics that have been emerging from the most recent MJO studies (e.g., Kim et al. 2014; Sobel et al. 2014). That is, 1) the radiative heating and surface fluxes destabilize the MJO disturbance by amplifying and maintaining MJO MSE anomalies, while 2) the vertical advection stabilizes the disturbance by exporting MSE, and 3) the horizontal advection plays a significant role in the eastward propagation by building up moist conditions ahead and providing dry conditions behind the active convective phase. These points are investigated in the MJO events during TOGA COARE.

Neelin and Held (1987) introduced a normalized version of the vertical advective term, known as the gross moist stability, which ''provides a convenient way of summarizing our ignorance of the details of the convection and large-scale transients.'' Other versions of this quantity have been used in many studies [see a review paper by Raymond et al. (2009)]. In this work, we examine the implications of the bottom-heavy–top-heavy evolution of vertical motion profiles for the gross moist stability. We also briefly discuss an appropriate choice of time filters for investigating relatively high-frequency variability in the TOGA COARE dataset.

Section 2 describes our data and filtering, regression methodology. In section 3, we show column-integrated MSE budgets for various time scales of variability as well as vertical motion profiles. Section 4 has a discussion of gross moist stability and calculations of this quantity. In section 5, we discuss the relationship between a constant gross moist stability and the vertical motion structure being well described by a first baro clinic mode. In this section, we estimate the gross moist stability in a different way from section 4 and also briefly discuss sensitivity to our filter choice. In section 6, we describe our conclusions.

2. Data and methodology

a. Data description

We investigated the data associated with the column-integrated moist static energy budget equation during TOGA COARE (Webster and Lukas 1992). TOGA COARE is a package of various field experiments conducted in the western equatorial Pacific. The experiment provided detailed observations of the mean and transient states of the tropical variability in the western Pacific warm pool, enabling identification of the dominant dynamical and thermodynamic processes in large-scale tropical convective systems. We utilized the data during the intensive operative period (IOP) from 1 November 1992 to 28 February 1993 with 6-hourly time resolution. Each variable was averaged over the spatial domain called the intensive flux array [IFA; see Fig. 14 in Webster and Lukas (1992)].

[1] Since most of the diabatic heating is balanced by vertical DSE advection and profiles of the DSE are relatively constant in the tropics, structures of the diabatic heating are similar to those of the vertical velocity profiles.

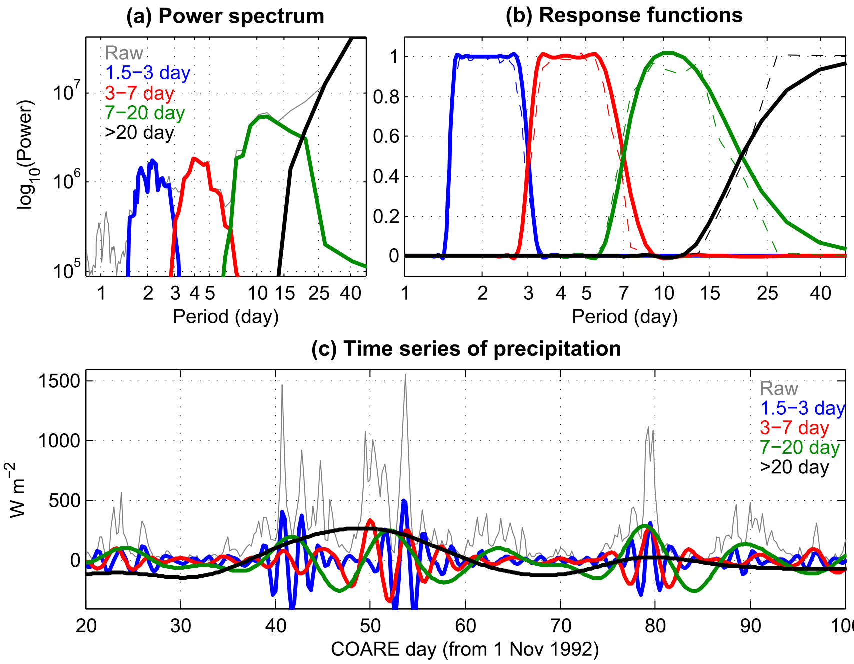

FIG. 1. (a) Power spectra of raw and filtered precipitation. Raw, ~2-, ~5-, ~10-, and >20-day (MJO) time scales are illustrated in gray, blue, red, green, and black lines, respectively. (b) Response functions of Lanczos filters with different cutoff frequencies. The colors are as in (a). Thick solid lines represent theoretical responses of the filters and thin dash lines show computed responses from the precipitation spectra. (c) Time series of raw and filtered anomalous precipitation. The black line shows two MJO events during TOGA COARE.

The dataset we used was objectively constructed by Minghua Zhang, who used constrained variational analysis for producing each variable. That method guarantees the conservation of the column-integrated mass, water, and DSE. See Zhang and Lin (1997) for more detailed description about the constrained variational analysis.

b. *Selection of time scales*

For examining the column MSE budgets and associated terms for different frequencies of variability, we chose four time scales: ~2-day, ~5-day, ~10-day, and MJO (>20 day) time scales. Those time scales are chosen based on a power spectrum of the precipitation during TOGA COARE and previous TOGA COARE studies. Figure 1a shows the power spectrum of the precipitation. Since the purpose of this study is not to investigate spectral signals that have been already examined by many previous studies, we will not look at statistical robustness of the signals in the power spectrum. We will use this power spectrum just for the purpose to determine which time scales should be separated to be investigated.

Figure 1a shows that there are four peaks with different periodicities. The first one is the diurnal cycle, which is not of our interest in this study and thus was removed by filtering in the analysis. The second peak can be found around the 2-day period. This signal has been investigated by Takayabu et al. (1996) and Haertel and Kiladis (2004), who have pointed out that there exist westward-propagating 2-day inertia–gravity waves during TOGA COARE. Thus, we dealt with this time scale separately. The other signals are found around the 4–5- and 10–13-day periods, which could be Kelvin wave signals. Because those two are obviously distinct and different from the 2-day wave signal, we also examined those time scales separately. Because the signal of the 10–13-day period in the power spectra is much smaller than the other signals, we cannot negate the possibility that the signal here is just a statistical noise. Nevertheless, we investigate this signal in order to keep consistency with Mapes et al. (2006), who have also investigated this periodicity in the TOGA COARE dataset. Finally, the MJO time scale was extracted because many previous studies have shown there are two MJO events during TOGA COARE (e.g., Velden and Young 1994; Lin and Johnson 1996; Yanai et al. 2000; Kikuchi and Takayabu 2004) in late November–December (around 30–65 COARE days) and in February (around 70–100 COARE days). Because the second MJO signal was attenuated before reaching the IFA [see Fig. 3 in Yanai et al. (2000)], most of the features in the following analyses on the MJO time scale reflect the structures of the first MJO event.

c. Filtering

To extract different time-scale features, a Lanczos filter was utilized. This filter has been popularly used in meteorology and other areas because the responses of frequencies to the filter has been well studied (Duchon 1979) and it has desirable behaviors with minimum Gibbs oscillations and relatively sharp cutoff slopes that prevent frequencies of interest from being contaminated by undesirable leakage of frequencies and artificial false responses produced by the Gibbs oscillations. We will briefly discuss sensitivities of the results to the choice of filtering in section 5d, where we will compare the Lanczos filter with a running-mean filter, especially on short time scales.

There is a common tradeoff between the number of weightings, or the number of data points that have to be sacrificed, and desirable behaviors of the filter. We chose 151 as the number of the weightings for all the analyses. This number was chosen in such a way that the response function of the filter looks appropriate enough to separate the MJO signals from the other shorter-time-scale signals (see Fig. 1b). Although we could have used a smaller number for the analyses on the shorter time scales (~2- and ~5-day scales) for reducing sacrificed points, we used the same number for all the analyses. We tried different numbers of weightings, and found that those did not make significant changes in the results. Figure 1c shows time series of the raw and filtered precipitation. We can see one strong MJO signal from around 30 November 1992 to 3 January 1993 (from 30 to 65 COARE days) and one weak signal from around 8 January to 7 February 1993 (from 70 to 100 COARE days).

d. Regression analysis and correlation test

Variability on the different time scales was plotted using a linear lag regression analysis. This method has been used by many studies (e.g., Kiladis and Weickmann 1992; Mapes et al. 2006). In this analysis, a predictand is regressed against a predictor (or a master index) to determine regression slopes at different lag times. These computed regression slopes are scaled with one standard deviation of the predictor so that the computed regression slopes have the same unit as that of the predictand. We chose precipitation as the predictor and each variable in Eq. (1) as a predictand. We also computed the vertical structures of the regression slopes of vertical pressure velocity ω, wind divergence, and specific humidity on the different time scales as in Mapes et al. (2006). Those slopes were computed at each lag time and each height. Both the predictor and predictands were filtered with a Lanczos filter for statistical correlation tests. (For a regression analysis, predictands do not need to be filtered.)

Statistical correlation tests were applied to test whether a given feature is statistically significant. Degrees of freedom (DOF) for the correlation tests were estimated at each lag and height following Bretherton et al. (1999). Although the values of the estimated DOF vary among different grids and variables, those variations are small enough that we neglect them. The DOF on the ~2-day time scale is about 102 (this is an average value of the different values of the DOF) and the DOF on the ~5-day time scale is about 22. On the ~10-day time scale, the number of different realizations (convection) can be counted in Fig. 1c and it is about 6; thus, the DOF for the correlation test on this time scale is 4. For the MJO time scale, there are only two independent events. Since those numbers of the independent samples on the ~10-day and the MJO time scales are too small to do statistical tests, statistical significance was tested only on the ~2- and ~5-day time scales.

3. Results: Column MSE budgets and omega profiles

a. Column MSE budgets

In the top panels of Fig. 2, plotted are lag autocorrelations of precipitation, lag correlations between precipitation and column-integrated MSE, and in the bottom panels lag regression slopes of each term in Eq. (1) regressed against the precipitation and scaled with one standard deviation of the precipitation on the different time scales. The standard deviations of raw data, the ~2-day, the ~5-day, the ~10-day, and the MJO time scales, are 229, 112, 91, 121, and 123 W m^{-2}, respectively. Every variable is filtered with a Lanczos filter on the corresponding time scales. Confidence intervals of the 90% significant level of the regression slopes are also plotted on the bottom-left corners on only the ~2-day and ~5-day time scales—the time scales on which we can get enough DOF. The values of confidence intervals differ at different lags; thus, average values among the lag time windows are plotted. The numbers on the right corners of each subplot are average values (among the lag time windows) of the numbers of the independent samples. Increased errors on the ~5-day time scale compared with the ~2-day time scale are primarily due to the reduced DOF.

We first acknowledge that because of the lack of DOF we are uncertain about whether Figs. 2c and 2d represent statistically significant features of the MSE budgets on those time scales. To examine statistical significance

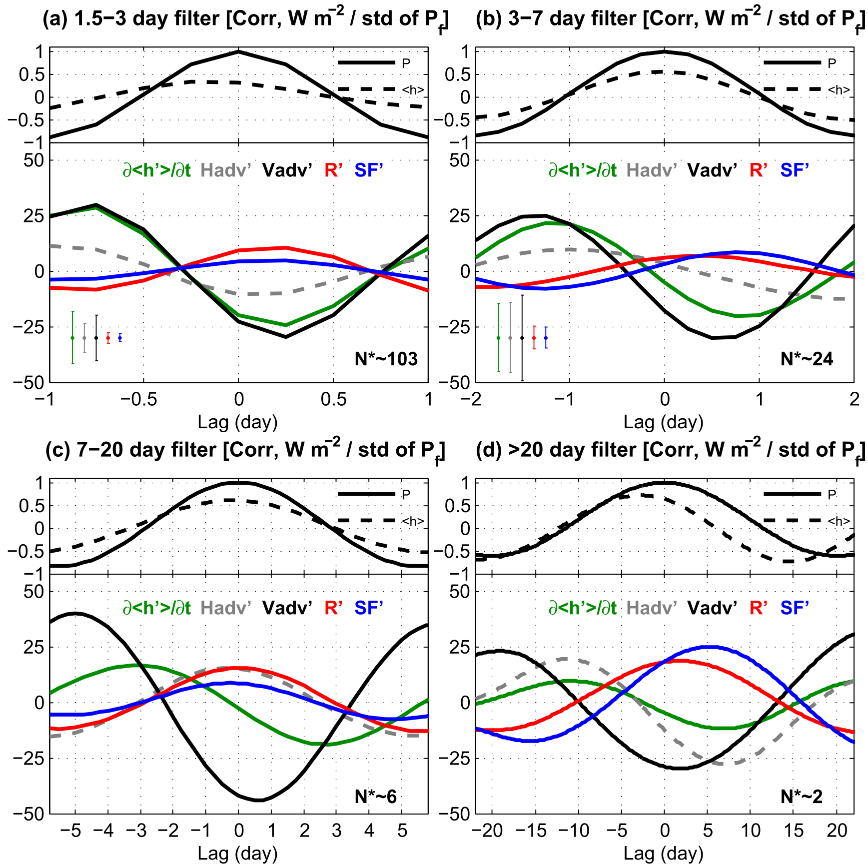

FIG. 2. (a)–(d) (top) Lag autocorrelations of filtered precipitation (solid lines) and lag correlations between filtered precipitation and filtered column MSE (dashed lines) on the four different time scales. (bottom) Regression slopes of anomalies of $\partial\langle h\rangle/\partial t$ (green), $-\langle \mathbf{v}\cdot\nabla h\rangle$ (gray dash), $-\langle \omega\partial h/\partial p\rangle$ (black), $\langle Q_R\rangle$ (red), and SF (blue), regressed against filtered precipitation and scaled with one standard deviation of the filtered precipitation on the different time scales. The precipitation was filtered with (a) 1.5–3-day bandpass, (b) 3–7-day bandpass, (c) 7–20-day bandpass, and (d) >20-day low-pass filters. The error bars in the left-bottom corners in (a) and (b) represent average values (among the lag time windows) of significant errors for each MSE budget term computed with 90% significant level. The numbers in the right-bottom corners show estimated independent sample sizes on the different time scales.

on those time scales, we need to investigate longer time series than the TOGA COARE data, which is left for future work. Nevertheless, we can see that the patterns in Fig. 2d for the MJO events during TOGA COARE are similar to those in Fig. 10 in Benedict et al. (2014) in which 10-yr-long ERA-Interim and TRMM with objectively analyzed surface flux data were investigated.

Column-integrated radiative heating $\langle Q_R\rangle$ is approximately in phase with the precipitation (or the precipitation leads slightly) on all the time scales. Surface fluxes lag the precipitation peaks on all the time scales except for the ~10-day scale for which both radiative heating and surface fluxes are nearly in phase with the precipitation. The lags of SF are significant on the ~5 day and MJO time scales (>20 day).

The behaviors of column-integrated vertical MSE advection ($-\langle \omega\partial h/\partial p\rangle$) differ among the time scales. On the ~2-day scale, positive advection (i.e., import of h) leads the precipitation and the minimum value (i.e., maximum export of h) lags the precipitation peak. The tendency of column-integrated h ($\partial\langle h\rangle/\partial t$) agrees with the vertical advection term, which implies that on this time scale most of the recharge–discharge cycle of h is explained by the vertical advection while the other terms cancel each other out.

On the ~5-day scale, the pattern of vertical advection term is similar to that of the ~2-day scale in which positive advection leads the precipitation and negative advection lags the precipitation peak. Unlike the ~2-day scale, there is a lag between the vertical advection and tendency term on this time scale, which is due to negative contributions of the radiative heating and surface fluxes in the early stage of the convection. This lag between the vertical advection and tendency terms becomes larger as the time scale gets longer.

On the ~10-day scale, the maximum vertical advection leads the tendency maximum by around 3 days. Furthermore, the relative amplitude of vertical advection to the tendency term becomes greater on this time scale, which is due to the other terms that work in the opposite way to the vertical advection. That is, in the early stage of the convection the vertical advection recharges h while the other terms discharge h, and in the mature stage the vertical advection exports h while the other terms recharge it.

On the MJO time scale, akin to the ~10-day scale, the positive vertical advection leads the positive tendency term and amplitude of the vertical advection is greater than that of the tendency term because the other terms play significant roles in the h budgets. It is also worthwhile to note that as the time scale gets longer, the vertical advective export of MSE (i.e., $+\langle\omega\partial h/\partial p\rangle$) becomes more in phase with the precipitation peak (i.e., the lag relation becomes closer to 180° out of phase). On ~2-day and ~5-day time scales, the vertical advective h export lags the precipitation peak, while on the ~10-day and MJO time scales it becomes more in phase with the precipitation peak. This in-phase h export pattern has implications when we consider the gross moist stability (GMS), which will be discussed in section 4b.

The horizontal advection (i.e., $-\langle\mathbf{v}\cdot\nabla h\rangle$) exhibits significantly different behaviors among these different frequencies. On the ~2-day scale, the positive horizontal advection leads the precipitation and the minimum value is reached slightly after the precipitation peak. The horizontal advection acts in almost opposite ways to the radiative heating and surface fluxes. As a result, those terms cancel each other out. On the ~5-day scale, the horizontal advection is almost 90° out of phase with the precipitation. In contrast, on the ~10-day scale, it is almost in phase with the precipitation. Again, since Fig. 2c contains only six independent samples, we cannot conclude that this pattern is statistically robust. More detailed investigations should be done on this time scale in future work. On the MJO time scale, the horizontal advection is 90° out of phase with the precipitation. Before the precipitation peak, the horizontal advection imports h, while after the precipitation maximum, it exports the h. As the time scale gets longer, the amplitude of the variations of the horizontal advection become greater, which might indicate that the relative contribution of the horizontal advection to the recharge and discharge of the MSE becomes more important as the time scale gets longer.

The relative amplitudes of each term indicate which terms are the most important for these frequencies. For all the frequencies except for the MJO, the vertical advection dominates the other terms, which implies that the vertical advection is the most important h sink and source. At longer time scales of variability (lower frequencies), however, the amplitude of the vertical advection term relative to the source–sink terms becomes less. On the MJO scale, the horizontal and vertical advection, radiative heating, and surface fluxes all have relatively similar amplitudes. That indicates that all the terms in the MSE budgets play important roles in the MJO dynamics.

Furthermore, the results shown in Fig. 2d on the MJO time scale reinforce the view of the MJO dynamics that has been emerging from recent studies (e.g., Kim et al. 2014; Sobel et al. 2014). That is, 1) the radiative heating and surface fluxes amplify and maintain the MJO MSE anomalies while 2) the MJO disturbance is stabilized by the vertical advection that exports MSE and cancels the effect of the radiative heating and surface fluxes, and therefore 3) the eastward propagation of the MJO is primarily driven by the horizontal advection which provides moistening ahead (in the negative lags, or to the east of), drying behind (in the positive lags, or to the west of) the active convective phase. Although there are differences between the different MJO events as pointed out by Sobel et al. (2014), our results, in general, show significant consistencies with the results given by Kim et al. (2014) and, to some degree, with the results in Sobel et al. (2014).

b. Omega profiles

Figure 3 shows vertical structures of vertical pressure velocity and wind divergence on the different time scales. The areas surrounded by the green curves passed statistical correlation tests with 99% (on ~2-day time scale) and 80% (on ~5-day time scale) significant levels. The lower significance level used on the ~5-day time scale is because of smaller DOF on this time scale compared with the ~2-day time scale. The statistical tests were not applied for the ~10-day and MJO time scales owing to the lack of DOF. As Mapes et al. (2006) showed, we can observe tilting structures of the omega profiles in which the profile evolves from a bottom-heavy shape into a top-heavy shape (indicated by the black dash lines), and these tilting structures are statistically significant. The figures of the wind divergence illustrate the same information as the omega figures. Height of the lower-tropospheric convergence (blue contours) rises as the convection develops, making the tilting divergence profiles.

However, one can notice that the tilt of the omega profile becomes steeper as the time scale gets longer. Especially, on the MJO time scale, the contour line of omega is almost perpendicular to the isobaric surface at

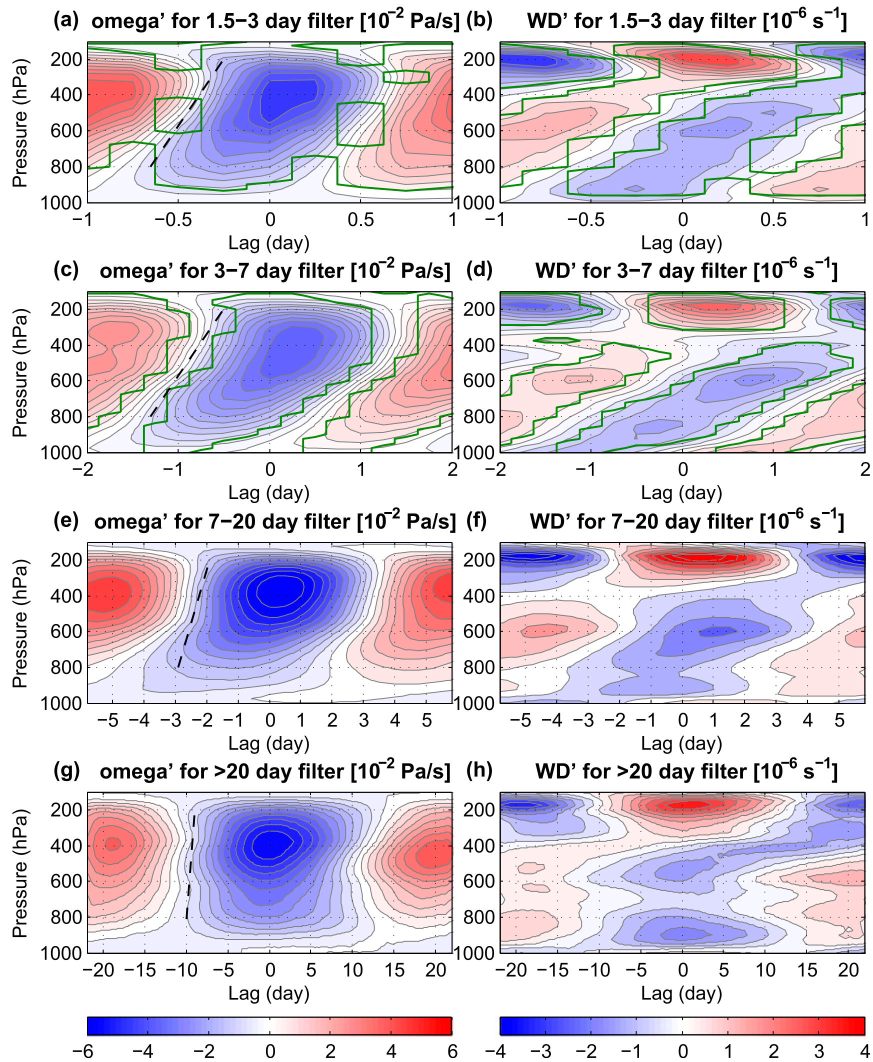

FIG. 3. Vertical structures of anomalous omega and wind divergence fields regressed against the filtered precipitation and scaled with one standard deviation of the filtered precipitation on (a),(b) ~2-, (c),(d) ~5-, (e),(f) ~10-, and (g),(h) >20-day scales. The contour interval of the omega plots is 0.6×10^{-2} Pa s^{-1}, and that of the wind divergence plots is 0.5×10^{-6} s^{-1}. The areas surrounded by the green lines in (a)–(d) correspond to the grids which passed correlation significance tests at the 99% (on the ~2-day scale) and 80% (on the ~5-day scale) levels. The black dashed lines illustrate tilting structures of the omega profiles on each time scale.

−10 lag days. There is a shallow convective phase on this scale, too (see from −22 to −12 lag days), but this shallow convection is more abruptly changed into deep convection compared with those on the shorter time scales in which the transitions of the convection from a bottom-heavy to a top-heavy shape happen more gradually. The divergence figures depict the differences among the time scales clearly. In the upper troposphere, the structures are qualitatively similar among the different time scales. In the inactive stage of the convection, strong convergence associated with upper-tropospheric descending motion happens at the top of the troposphere. In the mature stage of the convection, in contrast, strong divergence due to deep convection occurs.

In the lower half of the troposphere, differences among the time scales are prominent. On all the time scales except for the MJO time scale, in the inactive convective stage, the strongest divergence occurs around 600 hPa. On the MJO time scale, in contrast, the divergence at this level is much weaker than that on the shorter time scales, and the strongest divergence occurs around 900 hPa. This lower-tropospheric divergence maintains its strength until lag day −15. As this lower-tropospheric divergence disappears, the convection abruptly changes into deep convection.

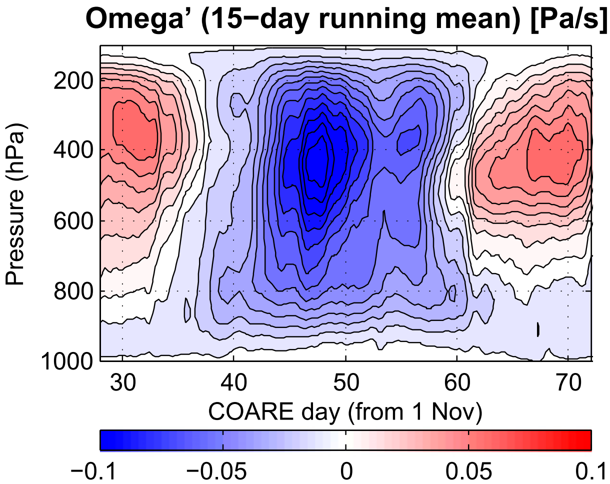

FIG. 4. Anomalous omega profiles of the first MJO event during TOGA COARE with a 15-day running-mean filter. The contour interval is 0.01 Pa s^{-1}.

Therefore, on the MJO time scale, the omega profiles behave like a single deep convection mode, which is often called a first baroclinic mode. This omega behavior has implications regarding the GMS of the convective system.

Before going to the next section, it should be emphasized again that the results shown in Figs. 3g and 3h reflect only two MJO events, one of which is a weak event, and thus it is almost a case study. Therefore, it is difficult to draw a general conclusion about the MJO structures from our analysis particularly because the details of the MJO structures differ significantly from event to event. However, we can at least claim that a strong tilt of the omega profile (or latent heating profile) is not necessary for the existence of the MJO, even though the tilt might play a role in the MJO dynamics.

Furthermore, it should also be noted that our lag regression methodology extracted the actual structures of the MJO event during TOGA COARE in an appropriate way. Figure 4 shows the time–height plot of the anomalous omega of the first MJO event during TOGA COARE, which occurs between ~30 and ~65 COARE days. In this plot, we simply utilized a 15-day running-mean filter. Although the contour is noisy as a result of the noise introduced by the running-mean filter, the overall structure is similar to that in Fig. 3g. This figure indicates that our methodology captures the MJO structures well and negates the possibility that the result shown in Fig. 3g is due to a false signal introduced by the statistical method.

4. More results: Gross moist stability

a. *GMS with different frequencies*

Now the GMS on the different time scales will be computed. Before doing actual computations, the concept of the GMS needs to be clarified. The GMS, which is a concept originated by Neelin and Held (1987), represents the efficiency of MSE export by convection and associated large-scale circulations. Raymond et al. (2009) defines a relevant quantity called normalized GMS (NGMS), which is a ratio of column MSE (or moist entropy) advection to intensity of the convection. Although different authors have used slightly different definitions of the NGMS (e.g., Fuchs and Raymond 2007; Raymond and Fuchs 2009; Raymond et al. 2009; Sugiyama 2009; Andersen and Kuang 2012), the physical implications behind those definitions are consistent in such a way that the NGMS represents efficiency of export of some intensive quantity conserved in moist adiabatic processes per unit intensity of the convection (Raymond et al. 2009). We employ one version of the NGMS defined as

$$\Gamma = \frac{\langle \mathbf{v}\cdot\nabla h\rangle + \left\langle \omega \dfrac{\partial h}{\partial p}\right\rangle}{\langle \mathbf{v}\cdot\nabla s\rangle + \left\langle \omega \dfrac{\partial s}{\partial p}\right\rangle}, \tag{2}$$

where h and s represent MSE and DSE, respectively. Since in the tropics, horizontal temperature gradients are negligible (weak temperature gradient; Sobel and Bretherton 2000), neglecting the horizontal DSE advection in the denominator yields

$$\Gamma = \frac{\langle \mathbf{v}\cdot\nabla h\rangle + \left\langle \omega \dfrac{\partial h}{\partial p}\right\rangle}{\left\langle \omega \dfrac{\partial s}{\partial p}\right\rangle}. \tag{3}$$

Equation (3) can be separated into horizontal and vertical components as

$$\Gamma = \Gamma_h + \Gamma_v, \tag{4}$$

where

$$\Gamma_h = \frac{\langle \mathbf{v}\cdot\nabla h\rangle}{\left\langle \omega \dfrac{\partial s}{\partial p}\right\rangle} \quad \text{and}$$

$$\Gamma_v = \frac{\left\langle \omega \dfrac{\partial h}{\partial p}\right\rangle}{\left\langle \omega \dfrac{\partial s}{\partial p}\right\rangle}.$$

In some NGMS studies, the vertical component of the NGMS Γ_v is simply called NGMS (or GMS) (e.g., Sugiyama 2009; Kuang 2011; Andersen and Kuang 2012; Sobel and Maloney 2012) while in the others, the horizontal component Γ_h is explicitly defined (e.g., Raymond and Fuchs 2009; Raymond et al. 2009; Benedict et al.

2014; Hannah and Maloney 2014; Sobel et al. 2014). Previous research has used Γ_v in various ways such as a diagnostic quantity in general circulation models (e.g., Frierson 2007; Hannah and Maloney 2011, 2014; Benedict et al. 2014), in observational data (e.g., Yu et al. 1998; Sobel et al. 2014),[2] as an output quantity of a MJO toy model (e.g., Raymond and Fuchs 2009), and as an input parameter of a MJO toy model (e.g., Sugiyama 2009; Sobel and Maloney 2012, 2013). As Hannah and Maloney (2011) and Masunaga and L'Ecuyer (2014) pointed out, values of Γ_v generally fluctuate in convective life cycles primarily as a result of variations of vertical velocity profiles (as seen in Fig. 3). Nevertheless, when used as an input parameter of a toy model, Γ_v is assumed to be a constant in the convective life cycle (e.g., Sugiyama 2009; Sobel and Maloney 2012). Furthermore, time-dependent fluctuations of the NGMS are also neglected when the NGMS is computed based on scatterplots between the numerator and denominator of the NGMS, which is one of the most general methods to compute the NGMS.

When considering NGMS on different time scales in data, we have to be careful about its interpretation. First of all, we can define a mean NGMS, in which we average the numerator and the denominator of Γ before taking the ratio. This is in keeping with the spirit of the definition. We can also define an anomalous NGMS, in which perturbations from the means of numerator and denominator are taken and the ratio of these perturbations is computed. Similarly, we can define a total NGMS.[3] It can be easily shown that the total NGMS is a constant if and only if the mean NGMS is equal to the anomalous NGMS. In many of previous studies, the total NGMS has been assumed to be constant. In such cases, one does not have to worry about the differences between the mean and anomalous NGMS. But when considering the total NGMS as a time-dependent variable, one should clarify which kinds of NGMS are being used: mean, anomalous, or total NGMS.

Furthermore, we can generalize the idea of the decomposition of NGMS from an aspect of Fourier transformation. By taking Fourier decomposition, Eq. (1) can be separated into

$$\frac{\partial \langle h \rangle_i}{\partial t} = -\langle \mathbf{v} \cdot \nabla h \rangle_i - \left\langle \omega \frac{\partial h}{\partial p} \right\rangle_i + \langle Q_R \rangle_i + \mathrm{SF}_i, \quad (5)$$

where subscripts represent a specific range of frequencies. For instance, $i = 0$ can be defined as the mean state, and $i = \mathrm{ISO}$ can be defined so that Eq. (5) represents intraseasonal oscillations as in Maloney (2009). Therefore, we can define NGMS on different time scales as

$$\Gamma_i = \frac{\langle \mathbf{v} \cdot \nabla h \rangle_i + \left\langle \omega \dfrac{\partial h}{\partial p} \right\rangle_i}{\left\langle \omega \dfrac{\partial s}{\partial p} \right\rangle_i}. \quad (6)$$

The horizontal and vertical components on different time scales can be defined similarly to Eq. (4).

Interpretations of the sign of the NGMS also require some attention. When dealing with bandpass filtered variability, the denominator of Eq. (6) represents anomalous quantities that can be both positive and negative. With a positive denominator—this is a usual case when convection is active—positive (negative) NGMS corresponds to export (import) of the MSE. But, when the denominator is negative, or when convection is inactive, the interpretation must be reversed; that is, a positive (negative) value corresponds to import (export) of the MSE.

b. NGMS during TOGA COARE

We estimated the time-dependent NGMS on the four different time scales using Eq. (6). Figure 5 shows the lag regression slopes of horizontal (blue), vertical (red), and combined (green) column-integrated MSE advection as a function of lag regression slopes of column-integrated vertical DSE advection on the different time scales. The elliptic shapes represent life cycles of convection in which each life cycle starts from a filled circle, going around counterclockwise, and terminates at a filled square. The values of Γ_h, Γ_v, and Γ at different convective phases can be estimated by computing the slopes of the lines that are drawn from the origin to the periphery of the elliptic shapes. For instance, on the ~2-day scale, Γ_v starts with a positive value (~0.2), which becomes larger and goes to infinity (this corresponds to the singularity of the NGMS). After passing through the singular point, it becomes negative, which grows into a positive value and reaches about 0.2 again at the peak of the convection. After the convective peak, Γ_v increases and becomes infinity again at the singular point, followed by negative values.

One conclusion we can draw from Fig. 5 is that the NGMS and all the components are not constant values on all the time scales, but they vary along the convective life cycle. But we can find that, as the time scale gets longer, Γ_v converges to a constant value around 0.2, which is the slope of the major axis of the elliptic shape. On the MJO time scale, the elliptic shape of the vertical

[2] In Yu et al. (1998), the computed quantity was GMS and a not normalized one.

[3] The phrase "total NGMS" is often used to refer to the combination of Γ_h and Γ_v. In this study, we use the phrase total NGMS to refer to the combination of the anomaly and mean state. The combination of Γ_h plus Γ_v is simply called NGMS or Γ in this paper.

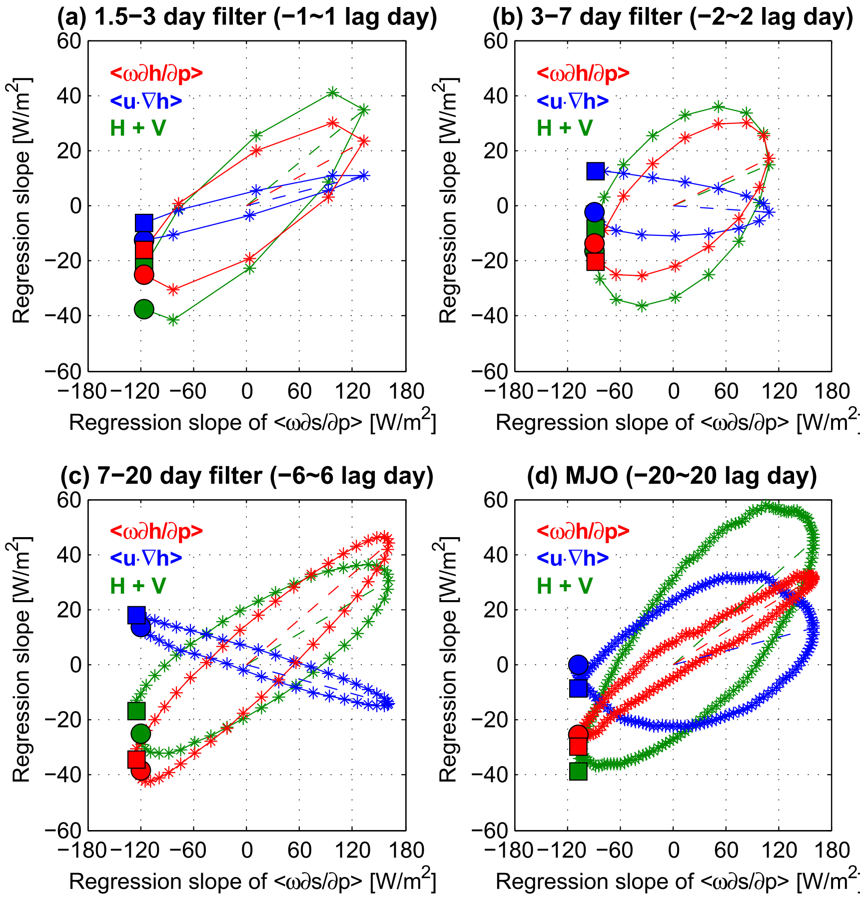

FIG. 5. Scaled lag regression slopes of vertical MSE advection (red), horizontal MSE advection (blue), and their combination (green) during convective life cycles as functions of scaled lag regression slopes of vertical DSE advection on different time scales. Each convective life cycle starts from a filled circle, going around counterclockwise and terminates at a filled square. The dashed lines illustrate Γ, Γ_h, and Γ_v at the precipitation peaks on different time scales that can be computed as the slopes of those lines.

MSE advection becomes very close to a linear shape (i.e., constant Γ_v) with the minor axis collapsed. This more-constant Γ_v is related to the fact that the column-integrated vertical MSE advection becomes closer to 180° out of phase (negatively in phase) with the precipitation as the time scale gets longer. This indicates that on longer time scales, the column-integrated vertical MSE advection is more linearly correlated to the precipitation. This result might support one of the popular usages of Γ_v in a MJO toy model in which Γ_v is assumed be a time-independent quantity (e.g., Sugiyama 2009; Sobel and Maloney 2012).

Compared with the vertical advection, the horizontal advection does not have a consistent pattern among the different time scales. On the ~2-day scale, the major axis of the ellipse of the horizontal advection has a positive slope while on the ~5-day scale the slope is almost zero. In contrast, on the ~10-day scales, it has a negative slope. On the MJO scale, its slope is slightly positive, but the values of Γ_h vary significantly during the convective life cycle. As a result, Γ (combination of Γ_h and Γ_v) also varies significantly during the convective life cycles on all the time scales. It should also be noted that the elliptic patterns of Γ are more similar to those of Γ_v than those of Γ_h on all the time scales except for the MJO time scale.

5. Discussion

a. Omega profiles and Γ_v

Most of the variations in $\langle \omega \partial h/\partial p \rangle$ are explained by the variations of the omega profiles (94% of the total variance in the TOGA COARE data), and the variations of the MSE profiles play a small role. We can use the assumption that omega profiles can be approximated by two dominant modal structures to reason about the

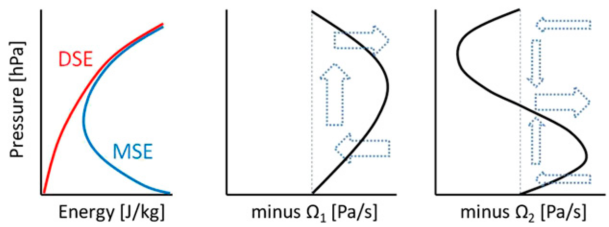

FIG. 6. Schematic figures of typical DSE and MSE profiles and shapes of the two dominant modes: Ω_1 and Ω_2. Arrows illustrate air flows of convection and associated large-scale circulations. Leftward (rightward) arrows correspond to convergence (divergence).

importance of each mode for the column MSE budget. We assume

$$\omega(t,p) \approx o_1(t)\Omega_1(p) + o_2(t)\Omega_2(p), \tag{7}$$

where Ω_1 and Ω_2 are often called first and second baroclinic modes, respectively, and o_1 and o_2 represent the time-dependent amplitudes of those modes. These could be any two modes that do a good job of describing the variability in vertical motion profiles, like those that come from a principle component analysis of vertical motion profiles. In the TOGA COARE data, the first mode of a principle component analysis (PCA) explains 71% of the variance, and the second mode explains 21% of the total variances of the omega profiles.

If we neglect the variations of the MSE profiles, we can represent Γ_v as

$$\Gamma_v \approx \frac{o_1\left\langle \Omega_1 \frac{\partial \overline{h}}{\partial p}\right\rangle + o_2\left\langle \Omega_2 \frac{\partial \overline{h}}{\partial p}\right\rangle}{o_1\left\langle \Omega_1 \frac{\partial \overline{s}}{\partial p}\right\rangle + o_2\left\langle \Omega_2 \frac{\partial \overline{s}}{\partial p}\right\rangle}, \tag{8}$$

where the bars represent the time averages.

In general, the MSE and DSE profiles, Ω_1 and Ω_2, if chosen via PCA, have the structures as shown in the schematic figure, Fig. 6. In the first baroclinic system, convergence happens in the lower troposphere, where the DSE is poor and divergence happens in the upper troposphere where the DSE is rich. Hence, in this system, strong net export of DSE happens (i.e., $\langle \Omega_1 \partial \overline{s}/\partial p\rangle$ is positive and large). In contrast, in the second baroclinic system, convergence happens both in the lower and upper troposphere, where the DSE is poor and rich, respectively, and divergence happens in the middle troposphere, where the DSE is moderate. As a result, the upper-tropospheric net import of DSE is canceled out by the lower-tropospheric net export of DSE, causing small value of $\langle \Omega_2 \partial \overline{s}/\partial p\rangle$. Consequently, the value of $\langle \Omega_1 \partial \overline{s}/\partial p\rangle$ is much larger than $\langle \Omega_2 \partial \overline{s}/\partial p\rangle$. Neglecting $\langle \Omega_2 \partial \overline{s}/\partial p\rangle$ in Eq. (8) yields

$$\Gamma_v \approx \frac{\left\langle \Omega_1 \frac{\partial \overline{h}}{\partial p}\right\rangle}{\left\langle \Omega_1 \frac{\partial \overline{s}}{\partial p}\right\rangle} + \frac{o_2}{o_1}\frac{\left\langle \Omega_2 \frac{\partial \overline{h}}{\partial p}\right\rangle}{\left\langle \Omega_1 \frac{\partial \overline{s}}{\partial p}\right\rangle}. \tag{9}$$

This equation shows that for this set of assumptions, time-dependent fluctuations Γ_v are due to the second term in the rhs of Eq. (9), which is the ratio of the amplitude of the second mode to that of the first mode times the ratio of the gross moist stability due to the second mode to the gross dry stability (the denominator of Γ_v; Yu et al. 1998) due to the first mode. In general, $\langle \Omega_2 \partial \overline{h}/\partial p\rangle$ is negative and large while $\langle \Omega_1 \partial \overline{h}/\partial p\rangle$ is positive and small (based on Fig. 6 and similar arguments to those for the gross dry stability $\langle \Omega_1 \partial \overline{s}/\partial p\rangle$ and $\langle \Omega_2 \partial \overline{s}/\partial p\rangle$). Thus, for this set of assumptions, the second term in the rhs of Eq. (9) is responsible for negative Γ_v in the early stage of the convection, as pointed out by Hannah and Maloney (2011) and Masunaga and L'Ecuyer (2014). This term is also responsible for the nonlinearity of the vertical MSE advection with respect to the convection, making the elliptic trajectories in Fig. 5. If this time-dependent term disappears, Γ_v given by Eq. (9) is the homomorphism of the GMS given by Neelin and Held (1987).

In Fig. 3, we showed that as the time scale gets longer, the tilting structure of the omega profile becomes less prominent. This disappearance of the tilt is likely due to smaller contributions of the second baroclinic mode on longer time scales compared with those on shorter time scales. This indicates that the second term in the rhs of Eq. (9) becomes smaller as the time scale gets longer, making Γ_v a more time-independent quantity. On shorter time scales where the second baroclinic mode is prominent, in contrast, the time-dependent term in Eq. (9) is robust, hence Γ_v on those time scales varies significantly in the convective life cycles.

Some studies have argued for an important role of shallow convection in the convective variability including the MJO in which shallow convection enhances moisture import via enhanced surface convergence and, thus, amplifies the convective system (e.g., Wu 2003; Kikuchi and Takayabu 2004). In our results, although it was less significant than the deep convective profile, a shallow convective phase can be observed even on the MJO time scale. That shallow convection could play a role in the MJO dynamics.

Interestingly, the elliptic trajectories shown in Fig. 5 have been already pointed out by Masunaga and L'Ecuyer (2014), who investigated the MSE budgets and computed the time evolution of the NGMS on short time scales using the satellite datasets. There are a few notable differences between our analysis and their study. First, they used a different NGMS definition,

TABLE 1. Values of $\overline{\Gamma}$, $\overline{\Gamma}_h$, and $\overline{\Gamma}_v$ on each time scale.

	Scale			
	~2 days	~5 days	~10 days	MJO
$\overline{\Gamma}$	0.26	0.25	0.20	0.33
$\overline{\Gamma}_h$	0.08	−0.02	−0.10	0.10
$\overline{\Gamma}_v$	0.18	0.25	0.29	0.20

which is a ratio of MSE advection to moisture advection instead of DSE advection. Therefore, their NGMS plot is a mirror image of our NGMS plot with respect to the x axis [see Fig. 13 in Masunaga and L'Ecuyer (2014)]. Second, they computed the total NGMS including the background state instead of the anomalous NGMS that we computed. Thus, the center of the elliptic shape is shifted to the right and downward. The composite methodology is also different from our study. Nevertheless, their study has drawn a similar conclusion about the NGMS variability to ours. That is, the first and second baroclinic modes respectively explain the larger (along the major axis) and smaller (along the minor axis) variability of the elliptic trajectory.

b. *How to compute NGMS*

The values of estimated NGMS depend on the method of the computation. In section 4, we showed the NGMS as a time-dependent variable. But in some recent NGMS studies, NGMS is computed based on a scatterplot of MSE advection as a function of DSE advection (e.g., Raymond and Fuchs 2009). In such a case, time-dependent fluctuations are not taken into account.

If we estimate the NGMS following that method, then the values of the NGMS and the horizontal and vertical components correspond to the slopes of the major axes of the elliptic trajectories in Fig. 5. The values of those slopes ($\overline{\Gamma}$, $\overline{\Gamma}_h$, and $\overline{\Gamma}_v$) are summarized in Table 1. As discussed above, $\overline{\Gamma}_h$ varies significantly among the time scales. Consequently, $\overline{\Gamma}$, which is the combination of $\overline{\Gamma}_h$ and $\overline{\Gamma}_v$, also varies among the different time scales. Although smaller than the variations of $\overline{\Gamma}$ and $\overline{\Gamma}_h$, there are variations of $\overline{\Gamma}_v$ among the time scales, too. These might be due to the variations of the shapes of Ω_1 among the different time scales, which could be caused by errors due to the small number of the independent samples.

c. *Tilt in other work*

Mapes et al. (2006, hereafter M06) proposed the "stretched building block" hypothesis that "individual cloud systems in different phases of a large-scale wave have different durations of shallow convective, deep convective, and stratiform anvil stages in their life cycles." This hypothesis was proposed to explain the apparent multiscale similarities of the vertical structures between the mesoscale convective systems, convectively coupled equatorial waves, and the MJO. The systematic steepening of the leading-edge slopes in the omega profiles shown in Fig. 3 suggest that omega may not have as much multiscale similarity as M06 suggested, especially on the MJO time scale.

The wind divergence field on the MJO time scale in our result (Fig. 3h) resembles that in M06 (the second panel of Fig. 8 therein), both of which contain a small amount of tilt. However, that tilt is, as shown in section 3b, too small to claim the multiscale similarity of the omega profiles, especially on the MJO time scale. In contrast, a significant multiscale similarity is observed in the specific humidity field. Figure 7 shows the time–height structures of specific humidity on the different time scales and there is significant tilt on all time scales, unlike in vertical motion. Our figure is consistent with Fig. 7 in M06, which is given as evidence for the vertical tilt in clouds on longer time scales. Hence, we conclude that tilt in the moisture field is more robust than that in the omega field on the MJO time scale.

Previous work is also suggestive of more tilt in diabatic heating than we are finding, during the TOGA COARE MJO. Specifically, our results can be compared with Fig. 9 in Lin et al. (2004, hereafter L04) and Fig. 12 in Kiladis et al. (2005, hereafter K05), in which the TOGA COARE dataset was analyzed in a similar lag regression method to ours. These studies examined diabatic heating (or Q1), which has a very similar structure to omega (not shown). The major difference in results between these studies and ours is found in the tailing edges of the event, where the L04 and K05 figures have more tilt. In Figs. 3 and 4, we show our lag regressed plot resembles the raw structure of the MJO with a simple time filter. We believe that the relevant difference in methodology between their work and ours is that both of the other studies used spatial filters in addition to time filters to obtain their index time series. Personal communication with Kiladis and Haertel confirmed that spatial filtering was used in their analysis and that the difference of time versus time–space filters makes nonnegligible differences in the diabatic heating structures.

d. *Sensitivity of choice of filter*

Finally, we will briefly discuss sensitivity of the choice of filters. Figure 8 illustrates the response functions of the >1.5-day low-pass Lanczos filter and daily-running-mean filter. This figure shows that by using the running-mean filter, about 60% of the signals on the 2-day scale are lost owing to the shallow slope of the response function. Even at a 4-day period that corresponds to the time scale of some of the Kelvin waves, about 20% of the signals are

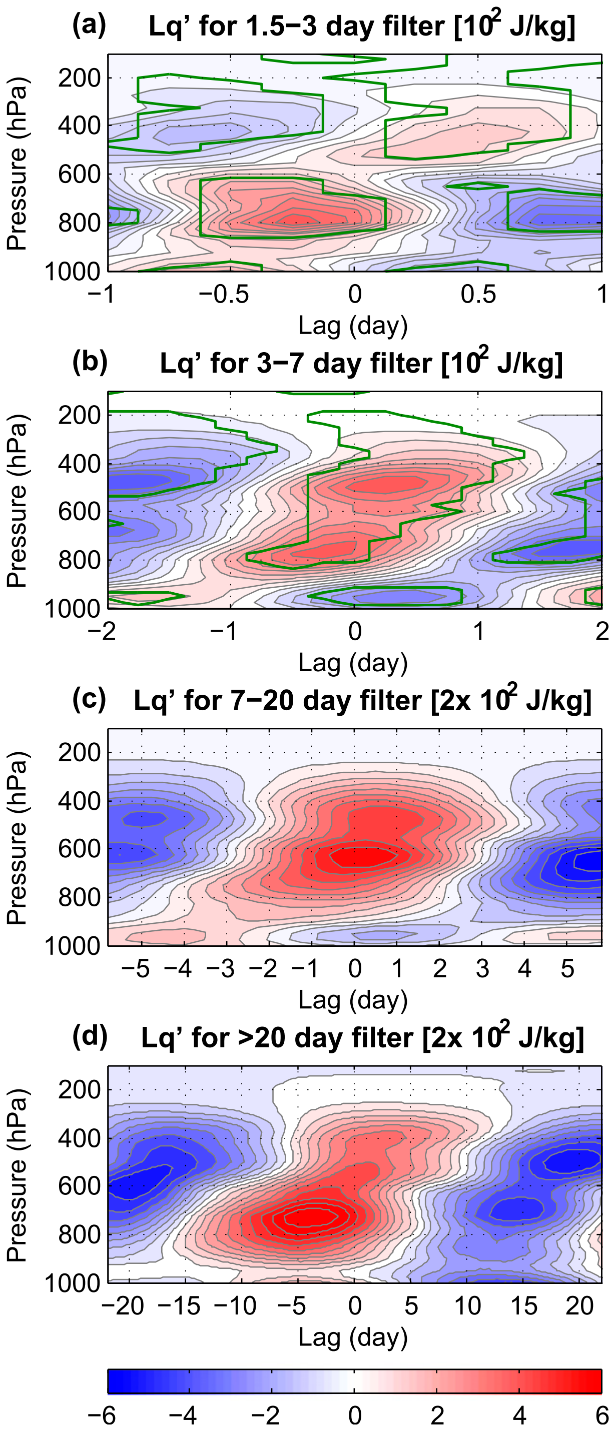

FIG. 7. As in Fig. 3, but for anomalous specific humidity. The contour intervals are 0.6×10^2 J kg^{-1} for (a) the ~2- and (b) the ~5-day scales and 1.2×10^2 J kg^{-1} for (c) the ~10-day and (d) the MJO scales.

lost. This indicates that for examining high-frequency variability such as inertia–gravity waves or Kelvin waves, the Lanczos filter with a steeper slope of the response function is more appropriate than the running-mean filter.

6. Conclusions

We have examined the column-integrated moist static energy (MSE) budget during the TOGA COARE field campaign using sounding data and filtering the data into various frequencies of variability with ~2-, ~5-, ~10-, and >20-day periodicity. In the deep tropics, fluctuations of the column MSE are primarily due to variations of column-integrated water vapor that are tightly connected with precipitation anomalies. Therefore, investigating the mechanisms of recharge and discharge of the column MSE leads us to a better understanding regarding the convective amplification and decay. Our analysis highlights the importance of the investigation of the column MSE on different time scales. We found that each budget term of the column MSE behaves in significantly different ways on the different time scales. As a result, dominant processes in the MSE recharge and discharge differ among the time scales. Some notable results are summarized as follows:

(i) On all the time scales except for the MJO time scale, the vertical MSE advection, $-\langle \omega \partial h/\partial p \rangle$, is the most dominant process with the greatest magnitude of variations in the MSE recharge–discharge mechanism.

(ii) On the shorter time scales (~2- and ~5-day scales), the vertical MSE advection accounts for most of the MSE recharge and discharge, and the other terms cancel out each other so that the tendency of the column MSE $\langle \partial h/\partial t \rangle$ is primarily explained by the vertical MSE advection.

(iii) As the time scale gets longer, the relative importance of the terms other than the vertical advection becomes greater. Especially on the MJO time scale, all the budget terms [horizontal advection, $-\langle \mathbf{v} \cdot \nabla h \rangle$, vertical advection, $-\langle \omega \partial h/\partial p \rangle$, radiative heating $\langle Q_R \rangle$, and surface fluxes (SF)] have nearly the same magnitude of variations.

(iv) The horizontal advection behaves in significantly different ways among the different time scales.

(v) The amplitude of the horizontal advection becomes greater as the time scale get longer, indicating that the horizontal advection plays a more important role in the MSE recharge–discharge mechanism on longer time scales than on shorter time scales.

(vi) The radiative heating is approximately in phase with the precipitation (or the precipitation leads slightly) while the surface fluxes lag the precipitation except for the ~10-day scale on which both the radiative heating and surface fluxes are approximately in phase with the precipitation.

(vii) On the shorter time scales, the MSE export via vertical advection (i.e., $+\langle \omega \partial h/\partial p \rangle$) lags the precipitation

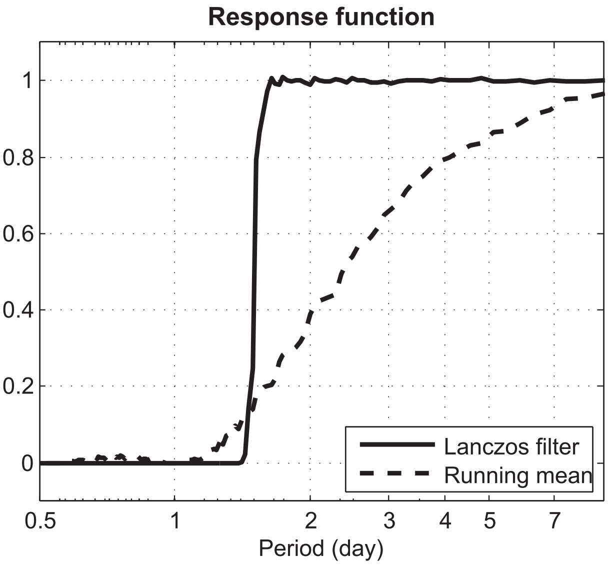

FIG. 8. Response functions of >1.5-day low-pass Lanczos filter (with 151 points of weightings) and daily running-mean filter.

peak. As the time scale gets longer, however, the MSE export becomes more in phase with the precipitation.

The last bullet of the summary above, more in-phase MSE export via vertical advection is primarily explained by variations in the omega profile. The tilt of the profile at the leading edge of the convection gets steeper as the time scale gets longer. This implies that the second baroclinic structure of the omega profile becomes less robust in the early stage of the convection. On the MJO time scale, the leading-edge tilt becomes very steep, and the overall omega structure becomes closer to the first baroclinic mode. Consequently, the vertical component of the normalized gross moist stability (NGMS) becomes more a constant quantity that is nearly independent of the convective life cycle. In contrast, on the shorter time scales where a second baroclinic mode is prominent, the vertical NGMS has large time dependency; thus, the values of the vertical NGMS vary significantly along the convective life cycle. The horizontal component of the NGMS does not have a consistent pattern among the different time scales since the horizontal MSE advection behaves in significantly different ways on the different time scales.

Furthermore, our results shown in Fig. 2d, the MSE budgets in the MJO event, reinforce the view of the MJO dynamics which has been emerging from recent MJO studies (e.g., Kim et al. 2014; Sobel et al. 2014) in the following ways: 1) The radiative heating and surface fluxes destabilize the MJO disturbance by amplifying and maintaining MSE anomalies. 2) The vertical advection stabilizes the disturbance by exporting the MSE and canceling the effects of the radiative heating and surface fluxes. 3) The horizontal advection plays a significant role in the eastward propagation by providing moistening ahead (in the negative lags, or to the east of) and drying behind (in the positive lags, or to the west of) the active phase. Although there are differences between the different MJO events, our results, in general, show significant commonalities with those viewpoints.

Finally, we should acknowledge again that we are uncertain about whether the results shown for the longer time-scale variability (~10-day and the MJO time scales) represent statistically significant patterns because of the lack of the degrees of freedom. Our results for the MJO time scale are broadly consistent with published work on MSE budgets observed during the DYNAMO field campaign by Sobel et al. (2014), though we find the vertical NGMS less variable over an MJO life cycle, possibly owing to our use of the Lanczos filter rather than a running mean. For more accurate and solid conclusions, we need to investigate more datasets such as ERA-Interim and TRMM, which contain much longer time series than the TOGA COARE data. We would also like to repeat our analysis using DYNAMO data in future work.

Acknowledgments. We thank Professor Gregory J. Tripoli and Professor Matthew H. Hitchman for reading Kuniaki Inoue's M.S. thesis describing this study. We also thank Professor Adam Sobel and Professor Hirohiko Masunaga for providing useful comments in a personal conversation. Useful and constructive comments from two anonymous reviewers that improved the original draft are gratefully acknowledged. Finally, we thank Dr. George N. Kiladis and Dr. Patrick T. Haertel, who kindly reproduced their Q1 structure plots and clarified our concern. This research is supported by NASA Grant NNX12AL96G.

REFERENCES

Andersen, J. A., and Z. Kuang, 2012: Moist static energy budget of MJO-like disturbances in the atmosphere of a zonally symmetric aquaplanet. *J. Climate,* **25,** 2782–2804, doi:10.1175/JCLI-D-11-00168.1.

Benedict, J. J., and D. A. Randall, 2007: Observed characteristics of the MJO relative to maximum rainfall. *J. Atmos. Sci.,* **64,** 2332–2354, doi:10.1175/JAS3968.1.

——, E. D. Maloney, A. H. Sobel, D. M. Frierson, and L. J. Donner, 2013: Tropical intraseasonal variability in version 3 of the GFDL atmosphere model. *J. Climate,* **26,** 426–449, doi:10.1175/JCLI-D-12-00103.1.

——, ——, ——, and D. M. W. Frierson, 2014: Gross moist stability and MJO simulation skill in three full-physics GCMs. *J. Atmos. Sci.,* **71,** 3327–3349, doi:10.1175/JAS-D-13-0240.1.

Bretherton, C. S., and P. K. Smolarkiewicz, 1989: Gravity waves, compensating subsidence and detrainment around cumulus clouds.

J. Atmos. Sci., **46,** 740–759, doi:10.1175/1520-0469(1989)046<0740:GWCSAD>2.0.CO;2.

——, M. Widmann, V. P. Dymnikov, J. M. Wallace, and I. Blad, 1999: The effective number of spatial degrees of freedom of a time-varying field. *J. Climate,* **12,** 1990–2009, doi:10.1175/1520-0442(1999)012<1990:TENOSD>2.0.CO;2.

——, M. E. Peters, and L. E. Back, 2004: Relationships between water vapor path and precipitation over the tropical oceans. *J. Climate,* **17,** 1517–1528, doi:10.1175/1520-0442(2004)017<1517:RBWVPA>2.0.CO;2.

Charney, J. G., 1963: A note on large-scale motions in the tropics. *J. Atmos. Sci.,* **20,** 607–609, doi:10.1175/1520-0469(1963)020<0607:ANOLSM>2.0.CO;2.

——, 1969: A further note on large-scale motions in the tropics. *J. Atmos. Sci.,* **26,** 182–185, doi:10.1175/1520-0469(1969)026<0182:AFNOLS>2.0.CO;2.

Cho, H., and D. Pendlebury, 1997: Wave CISK of equato rial waves and the vertical distribution of cumulus heating. *J. Atmos. Sci.,* **54,** 2429–2440, doi:10.1175/1520-0469(1997)054<2429:WCOEWA>2.0.CO;2.

Duchon, C. E., 1979: Lanczos filtering in one and two dimensions. *J. Appl. Meteor.,* **18,** 1016–1022, doi:10.1175/1520-0450(1979)018<1016:LFIOAT>2.0.CO;2.

Frierson, D. M. W., 2007: Convectively coupled Kelvin waves in an idealized moist general circulation model. *J. Atmos. Sci.,* **64,** 2076–2090, doi:10.1175/JAS3945.1.

Fu, X., and B. Wang, 2009: Critical roles of the stratiform rainfall in sustaining the Madden–Julian oscillation: GCM experiments. *J. Climate,* **22,** 3939–3959, doi:10.1175/2009JCLI2610.1.

Fuchs, Ž., and D. J. Raymond, 2007: A simple, vertically resolved model of tropical disturbances with a humidity closure. *Tellus,* **59A,** 344–354, doi:10.1111/j.1600-0870.2007.00230.x.

Haertel, P. T., and G. N. Kiladis, 2004: Dynamics of 2-day equatorial waves. *J. Atmos. Sci.,* **61,** 2707–2721, doi:10.1175/JAS3352.1.

——, ——, A. Denno, and T. M. Rickenbach, 2008: Vertical-mode decompositions of 2-day waves and the Madden–Julian oscillation. *J. Atmos. Sci.,* **65,** 813–833, doi:10.1175/2007JAS2314.1.

Hannah, W. M., and E. D. Maloney, 2011: The role of moisture–convection feedbacks in simulating the Madden–Julian oscillation. *J. Climate,* **24,** 2754–2770, doi:10.1175/2011JCLI3803.1.

——, and ——, 2014: The moist static energy budget in NCAR CAM5 hindcasts during DYNAMO. *J. Adv. Model. Earth Syst.,* **6,** 420–440, doi:10.1002/2013MS000272.

Kikuchi, K., and Y. N. Takayabu, 2004: The development of organized convection associated with the MJO during TOGA COARE IOP: Trimodal characteristics. *Geophys. Res. Lett.,* **31,** L10101, doi:10.1029/2004GL019601.

Kiladis, G. N., and K. M. Weickmann, 1992: Circulation anomalies associated with tropical convection during northern winter. *Mon. Wea. Rev.,* **120,** 1900–1923, doi:10.1175/1520-0493(1992)120<1900:CAAWTC>2.0.CO;2.

——, K. H. Straub, and P. T. Haertel, 2005: Zonal and vertical structure of the Madden–Julian oscillation. *J. Atmos. Sci.,* **62,** 2790–2809, doi:10.1175/JAS3520.1.

——, M. C. Wheeler, P. T. Haertel, K. H. Straub, and P. E. Roundy, 2009: Convectively coupled equatorial waves. *Rev. Geophys.,* **47,** RG2003, doi:10.1029/2008RG000266.

Kim, D., and Coauthors, 2009: Application of MJO simulation diagnostics to climate models. *J. Climate,* **22,** 6413–6436, doi:10.1175/2009JCLI3063.1.

——, J.-S. Kug, and A. H. Sobel, 2014: Propagating versus nonpropagating Madden–Julian oscillation events. *J. Climate,* **27,** 111–125, doi:10.1175/JCLI-D-13-00084.1.

Kuang, Z., 2008: A moisture-stratiform instability for convectively coupled waves. *J. Atmos. Sci.,* **65,** 834–854, doi:10.1175/2007JAS2444.1.

——, 2011: The wavelength dependence of the gross moist stability and the scale selection in the instability of column-integrated moist static energy. *J. Atmos. Sci.,* **68,** 61–74, doi:10.1175/2010JAS3591.1.

Lappen, C.-L., and C. Schumacher, 2012: Heating in the tropical atmosphere: What level of detail is critical for accurate MJO simulations in GCMs? *Climate Dyn.,* **39,** 2547–2568, doi:10.1007/s00382-012-1327-y.

——, and ——, 2014: The role of tilted heating in the evolution of the MJO. *J. Geophys. Res. Atmos.,* **119,** 2966–2989, doi:10.1002/2013JD020638.

Lin, J., B. Mapes, M. Zhang, and M. Newman, 2004: Stratiform precipitation, vertical heating profiles, and the Madden–Julian oscillation. *J. Atmos. Sci.,* **61,** 296–309, doi:10.1175/1520-0469(2004)061<0296:SPVHPA>2.0.CO;2.

——, and Coauthors, 2006: Tropical intraseasonal variability in 14 IPCC AR4 climate models. Part I: Convective signals. *J. Climate,* **19,** 2665–2690, doi:10.1175/JCLI3735.1.

Lin, X., and R. H. Johnson, 1996: Kinematic and thermodynamic characteristics of the flow over the western Pacific warm pool during TOGA COARE. *J. Atmos. Sci.,* **53,** 695–715, doi:10.1175/1520-0469(1996)053<0695:KATCOT>2.0.CO;2.

Maloney, E. D., 2009: The moist static energy budget of a composite tropical intraseasonal oscillation in a climate model. *J. Climate,* **22,** 711–729, doi:10.1175/2008JCLI2542.1.

Mapes, B. E., 2000: Convective inhibition, subgrid-scale triggering energy, and stratiform instability in a toy tropical wave model. *J. Atmos. Sci.,* **57,** 1515–1535, doi:10.1175/1520-0469(2000)057<1515:CISSTE>2.0.CO;2.

——, S. Tulich, J. Lin, and P. Zuidema, 2006: The mesoscale convection life cycle: Building block or prototype for large-scale tropical waves? *Dyn. Atmos. Oceans,* **42,** 3–29, doi:10.1016/j.dynatmoce.2006.03.003.

Masunaga, H., 2012: Short-term versus climatological relationship between precipitation and tropospheric humidity. *J. Climate,* **25,** 7983–7990, doi:10.1175/JCLI-D-12-00037.1.

——, and T. S. L'Ecuyer, 2014: A mechanism of tropical convection inferred from observed variability in the moist static energy budget. *J. Atmos. Sci.,* **71,** 3747–3766, doi:10.1175/JAS-D-14-0015.1.

Neelin, J. D., and I. M. Held, 1987: Modeling tropical convergence based on the moist static energy budget. *Mon. Wea. Rev.,* **115,** 3–12, doi:10.1175/1520-0493(1987)115<0003:MTCBOT>2.0.CO;2.

——, O. Peters, and K. Hales, 2009: The transition to strong convection. *J. Atmos. Sci.,* **66,** 2367–2384, doi:10.1175/2009JAS2962.1.

Peters, M. E., and C. S. Bretherton, 2006: Structure of tropical variability from a vertical mode perspective. *Theor. Comput. Fluid Dyn.,* **20,** 501–524, doi:10.1007/s00162-006-0034-x.

Raymond, D. J., 2000: Thermodynamic control of tropical rainfall. *Quart. J. Roy. Meteor. Soc.,* **126,** 889–898, doi:10.1002/qj.49712656406.

——, and Ž. Fuchs, 2009: Moisture modes and the Madden–Julian oscillation. *J. Climate,* **22,** 3031–3046, doi:10.1175/2008JCLI2739.1.

——, S. L. Sessions, A. H. Sobel, and Ž. Fuchs, 2009: The mechanics of gross moist stability. *J. Adv. Model. Earth Syst.,* **1,** 9, doi:10.3894/JAMES.2009.1.9.

Sobel, A. H., and C. S. Bretherton, 2000: Modeling tropical precipitation in a single column. *J. Climate,* **13,** 4378–4392, doi:10.1175/1520-0442(2000)013<4378:MTPIAS>2.0.CO;2.

——, and E. Maloney, 2012: An idealized semi-empirical framework for modeling the Madden–Julian oscillation. *J. Atmos. Sci.,* **69,** 1691–1705, doi:10.1175/JAS-D-11-0118.1.

——, and ——, 2013: Moisture modes and the eastward propagation of the MJO. *J. Atmos. Sci.,* **70,** 187–192, doi:10.1175/JAS-D-12-0189.1.

——, S. Wang, and D. Kim, 2014: Moist static energy budget of the MJO during DYNAMO. *J. Atmos. Sci.,* **71,** 4276–4291, doi:10.1175/JAS-D-14-0052.1.

Straub, K. H., and G. N. Kiladis, 2003: The observed structure of convectively coupled Kelvin waves: Comparison with simple models of coupled wave instability. *J. Atmos. Sci.,* **60,** 1655–1668, doi:10.1175/1520-0469(2003)060<1655:TOSOCC>2.0.CO;2.

Sugiyama, M., 2009: The moisture mode in the quasi-equilibrium tropical circulation model. Part I: Analysis based on the weak temperature gradient approximation. *J. Atmos. Sci.,* **66,** 1507–1523, doi:10.1175/2008JAS2690.1.

Takayabu, Y. N., K. Lau, and C. Sui, 1996: Observation of a quasi-2-day wave during TOGA COARE. *Mon. Wea. Rev.,* **124,** 1892–1913, doi:10.1175/1520-0493(1996)124<1892:OOAQDW>2.0.CO;2.

Velden, C. S., and J. A. Young, 1994: Satellite observations during TOGA COARE: Large-scale descriptive overview. *Mon. Wea. Rev.,* **122,** 2426–2441, doi:10.1175/1520-0493(1994)122<2426:SODTCL>2.0.CO;2.

Webster, P. J., and R. Lukas, 1992: TOGA COARE: The Coupled Ocean–Atmosphere Response Experiment. *Bull. Amer. Meteor. Soc.,* **73,** 1377–1416, doi:10.1175/1520-0477(1992)073<1377:TCTCOR>2.0.CO;2.

Wu, Z., 2003: A shallow CISK, deep equilibrium mechanism for the interaction between large-scale convection and large-scale circulations in the tropics. *J. Atmos. Sci.,* **60,** 377–392, doi:10.1175/1520-0469(2003)060<0377:ASCDEM>2.0.CO;2.

Yanai, M., S. Esbensen, and J.-H. Chu, 1973: Determination of bulk properties of tropical cloud clusters from large-scale heat and moisture budgets. *J. Atmos. Sci.,* **30,** 611–627, doi:10.1175/1520-0469(1973)030<0611:DOBPOT>2.0.CO;2.

——, B. Chen, and W. Tung, 2000: The Madden–Julian oscillation observed during the TOGA COARE IOP: Global view. *J. Atmos. Sci.,* **57,** 2374–2396, doi:10.1175/1520-0469(2000)057<2374:TMJOOD>2.0.CO;2.

Yu, J., C. Chou, and J. D. Neelin, 1998: Estimating the gross moist stability of the tropical atmosphere. *J. Atmos. Sci.,* **55,** 1354–1372, doi:10.1175/1520-0469(1998)055<1354:ETGMSO>2.0.CO;2.

Zhang, M. H., and J. L. Lin, 1997: Constrained variational analysis of sounding data based on column-integrated budgets of mass, heat, moisture, and momentum: Approach and application to ARM measurements. *J. Atmos. Sci.,* **54,** 1503–1524, doi:10.1175/1520-0469(1997)054<1503:CVAOSD>2.0.CO;2.